

Flow Matching Beyond Kinematics: Generating Jets with Particle-ID and Trajectory Displacement Information

Joschka Birk,^{1,*} Erik Buhmann,¹ Cedric Ewen,¹ Gregor Kasieczka,^{1,2} and David Shih³

¹*Institute for Experimental Physics, Universität Hamburg
Luruper Chaussee 149, 22761 Hamburg, Germany*

²*Center for Data and Computing in Natural Sciences (CDCS),
Universität Hamburg, 22176 Hamburg, Germany*

³*New High Energy Theory Center, Rutgers University
Piscataway, New Jersey 08854-8019, USA*

We introduce the first generative model trained on the JETCLASS dataset. Our model generates jets at the constituent level, and it is a permutation-equivariant continuous normalizing flow (CNF) trained with the flow matching technique. It is conditioned on the jet type, so that a single model can be used to generate the ten different jet types of JETCLASS. For the first time, we also introduce a generative model that goes beyond the kinematic features of jet constituents. The JETCLASS dataset includes more features, such as particle-ID and track impact parameter, and we demonstrate that our CNF can accurately model all of these additional features as well. Our generative model for JETCLASS expands on the versatility of existing jet generation techniques, enhancing their potential utility in high-energy physics research, and offering a more comprehensive understanding of the generated jets.

I. INTRODUCTION

Recently there has been considerable interest and activity in generative modeling for jet constituents. While showering and hadronization with standard programs such as PYTHIA [1] and HERWIG [2] is not a major computational bottleneck at the LHC [3], learning the properties of jets from data still has interesting potential applications. For example, generative modeling at the jet constituent level can be used to improve the performance of anomaly detection [4] techniques.

More generally, learning jets is an interesting laboratory for method development. In particular, it has been fruitful and effective to view the jet constituents as a high-dimensional point cloud, and to devise methods for point cloud generative models that incorporate permutation invariance. This route has led to a number of state-of-the-art approaches, recently explored in [5–14], that combine different permutation-invariant layers such as transformers [15] and the EPiC layer [7], with state-of-the-art generative modeling frameworks such as diffusion [16–20] and flow matching [21–24]. Successful models developed for jet point clouds can also potentially be adapted to other important point cloud generative modeling problems such as for fast emulation of GEANT4 [25–27] calorimeter showers [11, 13, 28, 29]. Finally, while event generation with generative models has concentrated primarily on low multiplicities and fixed structures [30–35], recent, in-principle permutation invariant, approaches exist as well [36, 37].

So far, efforts for jet generation have focused almost exclusively on the JETNET dataset of Refs. [38, 39]. Originally generated by [40], this dataset was subsequently adopted in the works of Ref. [5] as

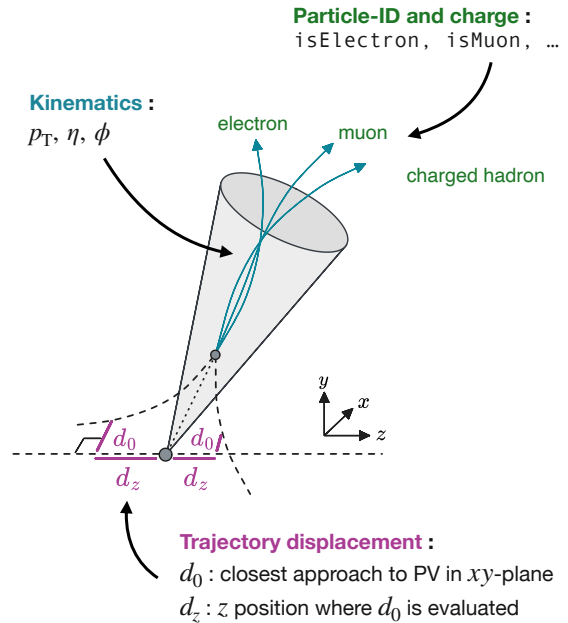


FIG. 1: Schematic overview of the different jet constituent features available in the JETCLASS dataset. The horizontal line at the bottom represents the beam axis and the circle on this line represents the primary vertex (PV).

a benchmark dataset for jet generative modeling. However, the JETNET dataset has a number of drawbacks that are readily becoming apparent. First, its limited size (180k jets per jet type) means there are not enough jets in JETNET to facilitate the training of state-of-the-art generative models as well as metrics such as the binary classifier metric [41, 42] which require additional training data. Second, JETNET uses small-radius ($R = 0.4$) jets (although the description in [5] incorrectly states a cone-size of $R = 0.8$ which is in disagreement with the observed angular distribution of constituents). This can lead

* joschka.birk@uni-hamburg.de

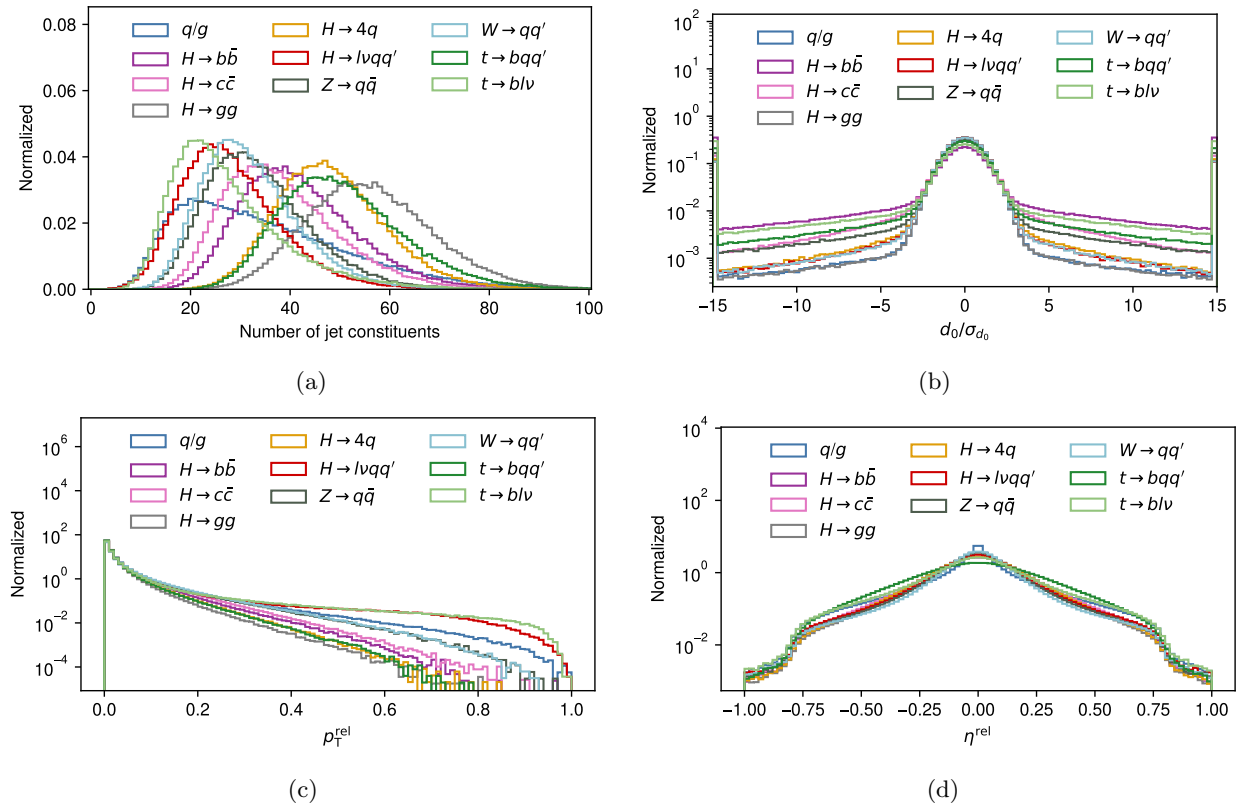


FIG. 2: Overview of some of the features from the JETCLASS dataset: (a) shows the number of jet constituents, (b) shows the significance of the transverse impact parameter d_0 , (c) shows the fraction of the jet p_T carried by the jet constituent and (d) shows the difference η^{rel} between the constituent pseudorapidity and the jet axis. The impact parameter significance d_0/σ_{d_0} is only shown for charged particles since the impact parameter is 0 for neutral particles. The number of jet constituents is a jet-level feature our model is conditioned on while the remaining features correspond to constituent-level features that our model generates.

to decay products not being fully contained in the jet, which can be seen e.g. in distributions such as the jet mass for top quarks, where there is a prominent secondary mass peak. Finally, JETNET focuses solely on the kinematics of the jet constituents, whereas there is a wealth of additional information inside the jets that could also be modeled, such as trajectory displacement, charge, and particle ID as illustrated in Figure 1.

In this work, we introduce the first generative model for jet constituents trained on the larger and more substantial JETCLASS dataset [43]. Other than demonstrating that existing techniques scale well to this new dataset, we also tackle new challenges introduced by the JETCLASS dataset, including the additional features mentioned above. We show that a single architecture consisting of a continuous normalizing flow (CNF) [44] constructed out of EPiC layers and trained with the flow matching technique [21–24] can learn to model all ten jet types and all features of JETCLASS well, both kinematics and beyond. Using the much larger statistics provided by JETCLASS we also train binary classifier metrics on the generative model for the first time, which allows us to further evaluate our results.

The rest of this paper is structured as follows:

Section II describes the JETCLASS dataset in more detail; Section III introduces the used generative model; Section IV provides an overview of the generative performance; and finally Section V concludes this work.

II. DATASET

We use the JETCLASS dataset [43], originally introduced in Ref. [45]. This dataset encompasses various features both on jet level and on jet constituent level for ten different types of jets initiated by gluons and quarks (q/g), top quarks (t), as well as W , Z , and H bosons. Jets initiated by a top quark or a Higgs boson are further categorized based on their different decay channels, resulting in the following ten categories: q/g , $t \rightarrow bqq'$, $t \rightarrow bl\nu$, $Z \rightarrow q\bar{q}$, $W \rightarrow qq'$, $H \rightarrow b\bar{b}$, $H \rightarrow c\bar{c}$, $H \rightarrow gg$, $H \rightarrow 4q$, and $H \rightarrow lvqq'$.

The jets are extracted from simulated events that are generated with MADGRAPH5_AMC@NLO [46]. Parton showering and hadronization is performed with PYTHIA [1] and detector effects are simulated with DELPHES [47] using the CMS detector [48] card. The jets are clustered with the anti- k_T al-

TABLE I: Features used for the studies in this paper. All features are either taken directly from the JETCLASS dataset or calculated from existing entries in the JETCLASS dataset. The model is conditioned on the jet features (first block) during generation. The remaining features are the constituent features our model is trained to generate.

Category	Variable	Definition
Jet features	Jet type	Indicating the type of the jet (i.e. $t \rightarrow bqq'$, q/g , ...)
	n_{const}	Number of constituents in the jet
	$p_{\text{T}}^{\text{jet}}$	Transverse momentum of the jet
	η^{jet}	Pseudorapidity of the jet
Kinematics	η^{rel}	Difference in pseudorapidity η between the constituent and the jet axis
	ϕ^{rel}	Difference in azimuthal angle ϕ between the constituent and the jet axis
	$p_{\text{T}}^{\text{rel}}$	Fraction of the constituent p_{T} and the jet p_{T}
Trajectory displacement	d_0	Transverse impact parameter value
	d_z	Longitudinal impact parameter value
	σ_{d_0}	Error of measured transverse impact parameter
	σ_{d_z}	Error of measured longitudinal impact parameter
Particle identification	charge	Electric charge of the particle
	isChargedHadron	Flag if the particle is a charged hadron ($ \text{pid} ==211$ or 321 or 2212)
	isNeutralHadron	Flag if the particle is a neutral hadron ($ \text{pid} ==130$ or 2112 or 0)
	isPhoton	Flag if the particle is a photon ($\text{pid}==22$)
	isElectron	Flag if the particle is an electron ($ \text{pid} ==11$)
	isMuon	Flag if the particle is a muon ($ \text{pid} ==13$)

gorithm [49] with a jet radius of $R = 0.8$. Jets are required to have a transverse momentum of $500 \text{ GeV} < p_{\text{T}}^{\text{jet}} < 1000 \text{ GeV}$ and a pseudorapidity of $|\eta^{\text{jet}}| < 2$. Furthermore, for all jets, except for the q/g jets, only those that contain all decay products of the boson or top quark are considered in the dataset.

Representative distributions of some of the features available in the JETCLASS dataset are presented in Figure 2, illustrating substantial distinctions among the various jet categories. As can be seen in Figure 2a, the dataset covers jet types with a large variety of number of jet constituents. Additionally, Figure 2b illustrates the expected tails of varying extents in the trajectory displacement. Notably, jet categories that do not include b quarks or c quarks have a rather narrow peak around 0, while jet categories that do include those types of quarks have a more spread out distribution, corresponding to the long lifetime of b - and c -hadrons.

The features that are used by our model are listed with the corresponding definitions in Table I. By conditioning our model on the jet type, we can train one model that is capable of generating all ten jet types. Furthermore, the jet transverse momentum $p_{\text{T}}^{\text{jet}}$ and the jet pseudorapidity η^{jet} are used as conditioning features in order to be able to obtain the non-relative constituent-level features after jet generation.

The kinematic features of the jet constituents are measured relative to the jet axis. i.e.

$$\eta^{\text{rel}} = \eta^{\text{const}} - \eta^{\text{jet}} \quad (1)$$

$$\phi^{\text{rel}} = \phi^{\text{const}} - \phi^{\text{jet}} \quad (2)$$

$$p_{\text{T}}^{\text{rel}} = p_{\text{T}}^{\text{const}} / p_{\text{T}}^{\text{jet}}. \quad (3)$$

The trajectory displacement features as well as the

discrete particle identification features are taken directly from the JETCLASS dataset. The jet constituents are assumed to be massless, as we do not include the particle energy in our model. In total, our model thus utilizes 13 constituent features to comprehensively characterize the constituents within generated jets. This set of features represents all available constituent features, from the JETCLASS dataset, with the only exception being the constituent energy.

III. MODEL

Overall, we follow the recent flow matching paradigm [21–24], using Gaussian probability paths as explained in Ref. [14].

The architecture of our model is based on the EPiC-FM model which was introduced in Ref. [14] with a few adjustments. It uses EPiC layers [7] to transform jet constituents as point clouds while preserving permutation symmetry. Besides the point cloud, EPiC layers also take as input a global context vector, which learns to encode higher-level information about the whole point cloud by using both mean and sum aggregation over the points. The use of the global context vector is responsible for the computational efficiency of the EPiC layers – unlike the quadratic scaling for architectures that include edge features between all pairs of points (such as transformers), the computational cost of EPiC layers only scales linearly with the number of points.

A full list of the specific hyperparameters of the model is summarized in the Appendix in Table V. While the overall architecture is based on Ref. [14], it is scaled up for the JETCLASS dataset, with 20

EPiC layers instead of 6, an embedding dimension of 300 instead of 128, and a 16-dimensional global vector.

The jet-type conditioning is realized with a one-hot encoding, while the jet transverse momentum p_T^{jet} and jet pseudorapidity η^{jet} are used without any preprocessing. For jet generation, we fit a kernel density estimator (KDE) to the jet features (p_T^{jet} , η^{jet} , and n_{const}) for each jet type individually, and sample from the KDE to obtain the conditioning features and the number of constituents for the generated jets. For each jet, our model acts on a tensor of shape (N, C) , with $N = 128$ being the maximum number of jet constituents and C being the number of constituent features. To generate jets with fewer constituents ($n_{\text{const}} < 128$), we apply a binary mask throughout training; this ensures that the inputs and outputs of the EPiC layers are valid and in particular guarantees that the mean and sum aggregation steps within the EPiC layers are correctly normalized. The particle features are shifted to mean 0 and scaled to the same standard deviation. Furthermore, only particles with $|\eta^{\text{rel}}| < 1$ are considered to remove a few particles in the tails of this distribution.¹

The model is trained for 500 epochs with a training sample size of 3M jets (300 000 jets per jet type).²

The AdamW optimizer [50] is used with a maximum learning rate of 0.001 and weight decay of 5×10^{-5} . The learning rate is scheduled with a cosine-annealing learning rate scheduler with a linear warm-up period over 20 epochs. The model after the last epoch is chosen for evaluation.³ For the jet generation, we use the midpoint ODE solver, a 2nd order Runge-Kutta variant. After jet generation, the p_T^{rel} values of the generated jet constituents are clipped to the minimum and maximum values that are found in the training dataset. Furthermore, the electric charge is rounded to the nearest integer within $\{-1, 0, 1\}$. The remaining discrete particle-identification features are post-processed with an argmax operation such that the particle-ID feature with the maximum value is set to 1 and the remaining ones are set to 0. This ensures that generated particles are unambiguously assigned to one particle type. It should be noted that this might not be the

ideal handling of such discrete features, which could be improved and further investigated in future work. The model is implemented in PYTORCH [51] using PYTORCH LIGHTNING [52].

IV. RESULTS

In the following, we first evaluate the distributions of the constituent-level features that the model was trained on. Afterwards, we evaluate jet-level features that are derived from the constituent-level features, namely the jet mass, the N -subjettiness [53] ratios τ_{32} and τ_{21} as well as the D_2 [54] observable, which is a ratio of energy correlation functions [55]. Lastly, we train a binary classifier as in Ref. [41] to distinguish between real jets from the JETCLASS dataset and fake jets generated by our model, which allows us to evaluate the quality of the generated jets further.

For the evaluation of our model, we generate 5M jets (i.e. 500 000 jets per jet type) and evaluate the different feature categories separately. Instead of using the Wasserstein-1 distance as a metric for the agreement between the generated and the target distribution as in [5, 7, 8], we are following [14] and using the Kullback-Leibler (KL) divergence. As explained there, this metric choice is motivated by the fact that the Wasserstein-1 distance is well-suited for detecting distributions with different support, but can lead to misleading results for cases where the distributions have the same overlapping support but differ mainly in their shapes.

The KL divergence values are calculated by splitting the generated jets and the JETCLASS jets into 10 batches of 50 000 jets each and then calculate the reverse KL divergence for each batch. This allows us to evaluate the uncertainty of the KL divergence to be able to quantitatively compare it to the truth distribution. The reported values are the mean of those 10 individual KL divergence values and their standard deviation. For the truth values of the KL divergence, we take two independent samples of the test dataset and then calculate the KL divergence between those two samples using the same procedure as when comparing the real and generated jets. The bin edges of the binned probability distributions are constructed by calculating 100 equiprobable quantiles from the target distribution and setting the edges of the outermost bins to the minimum and maximum values found in the target distribution. Outliers of the distribution from the generated jets are put into the first and last bin.

A. Jet constituent modeling

A comparison of the kinematic features of the jet constituents is shown in Figure 3. For this comparison, we chose to compare $t \rightarrow bqq'$ jets and q/g jets, since those two types of jets have distinct characteristics in both the η^{rel} and the p_T^{rel} distribution.

¹ The jets in the JETCLASS dataset are reported to correspond to a jet radius of $R = 0.8$, but some jet constituents have $|\eta^{\text{rel}}| > 0.8$. However, most of the constituents fall into $|\eta^{\text{rel}}| \leq 0.8$, so only a very small fraction of jet constituents is removed by this cut.

² It should be noted that this is just a small fraction (3%) of the training jets available in the JETCLASS dataset. Training with more jets did not show significant improvements in some preliminary trials, so we limited the training set size to this small fraction of JETCLASS in this first study for the sake of minimizing the computational expense. We still benefited from the larger size of JETCLASS in that it enabled us to train the binary classifier metrics.

³ Given that the training of this model is very stable, the last epoch essentially also corresponds to the epoch with the lowest loss. Thus, for simplicity the model from the last epoch was chosen.

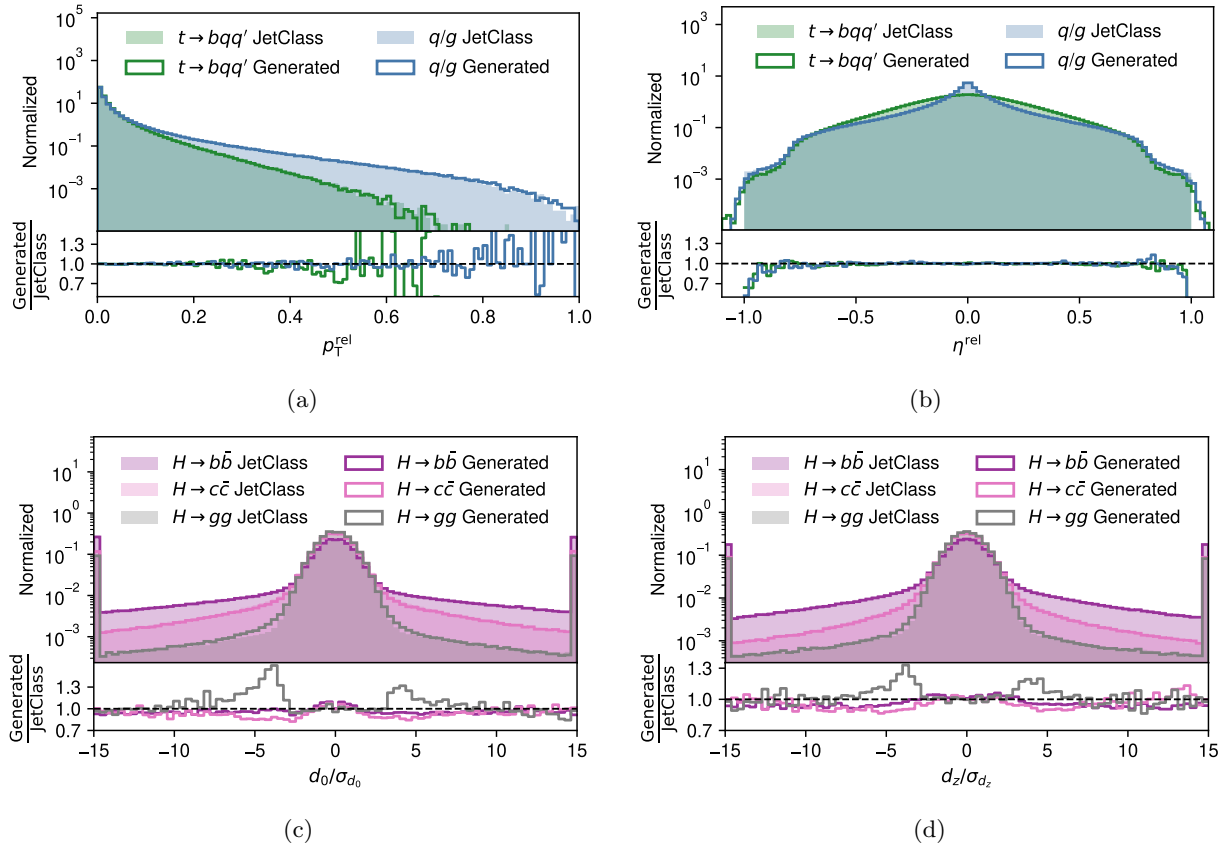


FIG. 3: Two kinematic features and the trajectory displacement of the jet constituents as generated by our model (solid lines) in comparison to the distributions obtained from the JETCLASS dataset (semi-transparent histograms). The upper row shows (a) the relative transverse momentum and (b) the relative pseudorapidity. The lower row shows (c) the transverse impact parameter significance and (d) the longitudinal impact parameter significance. Only charged particles are shown in the histograms of the trajectory displacement and the outermost bins show the underflow and overflow bins.

TABLE II: Kullback-Leibler divergence of constituent-level features with respect to the JETCLASS dataset.

	$ \text{KL}^{p_T^{\text{rel}}} (\times 10^{-3}) $	$ \text{KL}^{\eta^{\text{rel}}} (\times 10^{-3}) $	$ \text{KL}^{\phi^{\text{rel}}} (\times 10^{-3}) $	$ \text{KL}^{d_0/\sigma_{d_0}} (\times 10^{-3}) $	$ \text{KL}^{d_z/\sigma_{d_z}} (\times 10^{-3}) $
Truth (q/g)	0.06 ± 0.01	0.08 ± 0.01	0.07 ± 0.01	0.13 ± 0.01	0.11 ± 0.02
EPiC-FM (q/g)	0.073 ± 0.007	0.13 ± 0.02	0.12 ± 0.01	2.20 ± 0.06	3.72 ± 0.09
Truth ($H \rightarrow b\bar{b}$)	0.048 ± 0.004	0.07 ± 0.01	0.060 ± 0.008	0.10 ± 0.01	0.09 ± 0.01
EPiC-FM ($H \rightarrow b\bar{b}$)	0.071 ± 0.008	0.12 ± 0.02	0.12 ± 0.02	2.64 ± 0.09	1.47 ± 0.07
Truth ($H \rightarrow c\bar{c}$)	0.054 ± 0.007	0.07 ± 0.01	0.08 ± 0.02	0.11 ± 0.02	0.11 ± 0.02
EPiC-FM ($H \rightarrow c\bar{c}$)	0.078 ± 0.007	0.11 ± 0.02	0.134 ± 0.009	2.8 ± 0.1	1.96 ± 0.08
Truth ($H \rightarrow gg$)	0.034 ± 0.002	0.06 ± 0.02	0.053 ± 0.008	0.07 ± 0.01	0.07 ± 0.01
EPiC-FM ($H \rightarrow gg$)	0.057 ± 0.009	0.10 ± 0.01	0.10 ± 0.01	2.3 ± 0.1	3.5 ± 0.1
Truth ($H \rightarrow 4q$)	0.039 ± 0.005	0.057 ± 0.007	0.05 ± 0.01	0.08 ± 0.01	0.08 ± 0.02
EPiC-FM ($H \rightarrow 4q$)	0.057 ± 0.006	0.12 ± 0.02	0.11 ± 0.02	2.26 ± 0.07	3.2 ± 0.1
Truth ($H \rightarrow \ell\nu qq'$)	0.07 ± 0.01	0.10 ± 0.02	0.10 ± 0.01	0.14 ± 0.01	0.13 ± 0.02
EPiC-FM ($H \rightarrow \ell\nu qq'$)	0.10 ± 0.01	0.15 ± 0.02	0.137 ± 0.008	2.11 ± 0.08	2.61 ± 0.09
Truth ($Z \rightarrow q\bar{q}$)	0.061 ± 0.008	0.08 ± 0.01	0.08 ± 0.01	0.14 ± 0.03	0.13 ± 0.01
EPiC-FM ($Z \rightarrow q\bar{q}$)	0.07 ± 0.01	0.15 ± 0.02	0.13 ± 0.02	3.3 ± 0.2	2.1 ± 0.1
Truth ($W \rightarrow qq'$)	0.06 ± 0.01	0.088 ± 0.009	0.086 ± 0.008	0.12 ± 0.01	0.13 ± 0.02
EPiC-FM ($W \rightarrow qq'$)	0.082 ± 0.008	0.14 ± 0.02	0.13 ± 0.02	2.18 ± 0.05	2.6 ± 0.1
Truth ($t \rightarrow bqq'$)	0.043 ± 0.007	0.060 ± 0.005	0.057 ± 0.007	0.08 ± 0.01	0.08 ± 0.01
EPiC-FM ($t \rightarrow bqq'$)	0.08 ± 0.01	0.09 ± 0.01	0.10 ± 0.01	1.79 ± 0.07	1.8 ± 0.1
Truth ($t \rightarrow b\nu$)	0.07 ± 0.01	0.13 ± 0.02	0.15 ± 0.03	0.15 ± 0.02	0.15 ± 0.02
EPiC-FM ($t \rightarrow b\nu$)	0.11 ± 0.02	0.20 ± 0.03	0.19 ± 0.06	1.76 ± 0.09	1.46 ± 0.06

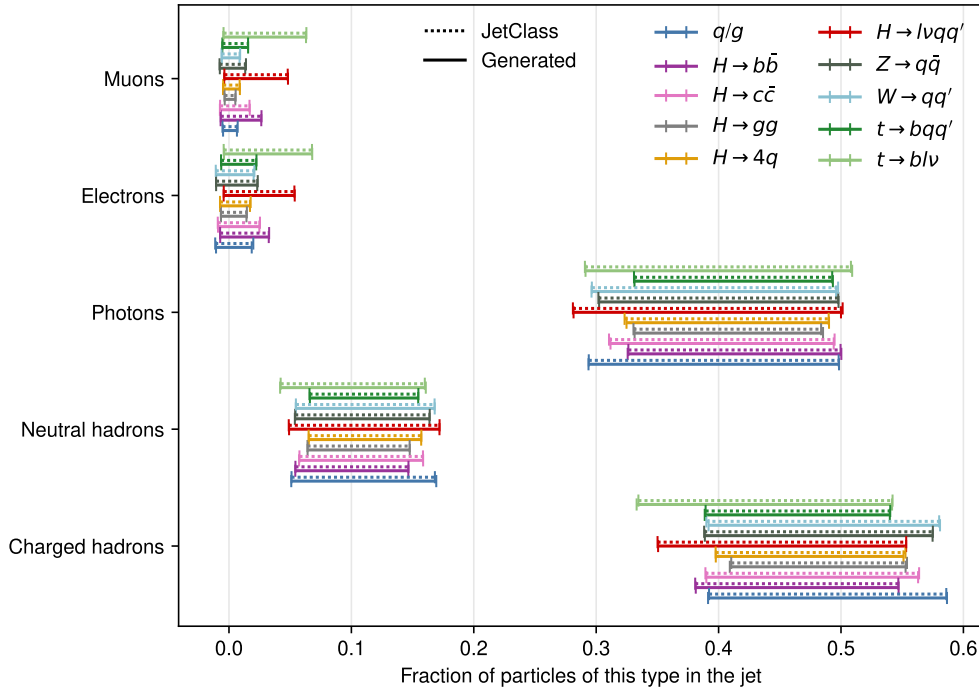


FIG. 4: Average fraction of jet constituents of different particle types. For each jet type, the intervals show the mean value over all evaluated jets with up and down variations of one standard deviation. The dotted lines show the values obtained for real jets from the JETCLASS dataset and the solid lines show the values obtained for the generated jets.

While particles in $t \rightarrow bqq'$ jets have on average a larger η^{rel} and thus have an overall wider η^{rel} distribution, q/g jets are more collimated, resulting in a sharper η^{rel} peak around $\eta^{\text{rel}} = 0$. Concerning the $p_{\text{T}}^{\text{rel}}$ distribution, $t \rightarrow bqq'$ jets are expected to show a smaller tail towards larger $p_{\text{T}}^{\text{rel}}$ values, since $t \rightarrow bqq'$ jets contain on average more constituents and thus the jet p_{T} is distributed over more particles, leading to smaller $p_{\text{T}}^{\text{rel}}$ values. The generated distributions of all three kinematic features agree very well with the corresponding distribution from the JETCLASS dataset, showing that our model is capable of generating jets of very different kinematic properties. This is also confirmed by the KL divergence values listed in Table II, which only have a small deviation from the truth values.

A comparison of the trajectory displacement modeling is shown in Figure 3 for $H \rightarrow b\bar{b}$, $H \rightarrow c\bar{c}$ and $H \rightarrow gg$ jets. Due to the long lifetime of b - and c -hadrons, the trajectory displacement of jet constituents associated with those hadrons is expected to be on average larger than for other jet constituents. Thus, the trajectory displacement distributions of $H \rightarrow b\bar{b}$ and $H \rightarrow c\bar{c}$ jets are expected to be wider than the trajectory displacement distribution of $H \rightarrow gg$ jets. Since the trajectory displacement is by definition zero for neutral particles in the JETCLASS dataset, only charged particles are considered in the histograms in Figure 3. For all three jet types, the histograms of the generated jets agree very well with the histograms of the real jets, showing that our model is capable of correctly modeling

the trajectory displacement of the jet constituents. Notably, our model is able to catch the essential differences between the trajectory displacement distributions of $H \rightarrow b\bar{b}$, $H \rightarrow c\bar{c}$ and $H \rightarrow gg$ jets, which is an important feature from the physics point of view. However, as seen both in the ratio panels in Figure 3 and in the corresponding KL divergence values in Table II, the agreement between the target distribution and the distribution obtained from the generated jets is worse for the impact parameter features than for the kinematic features, showing that the modeling of these distributions is more challenging. This could be further optimized in future work by choosing a different preprocessing for the impact parameter features, by e.g. transforming them using the hyperbolic tangent function, which would remove the large tails of the distributions.

The evaluation of the particle-ID modeling is shown in Figure 4, where we show the average fraction of jet constituents of different particle types for all ten jet types. For each jet type, the intervals show the mean value over all evaluated jets with up and down variation of one standard deviation. The agreement between the generated jets and the real jets is very good for all jet types, showing that on average the generated jets contain the same fraction of different particle types as the real jets. The modeling of the electric charge also shows very good agreement, which is shown in the Appendix in Section A.

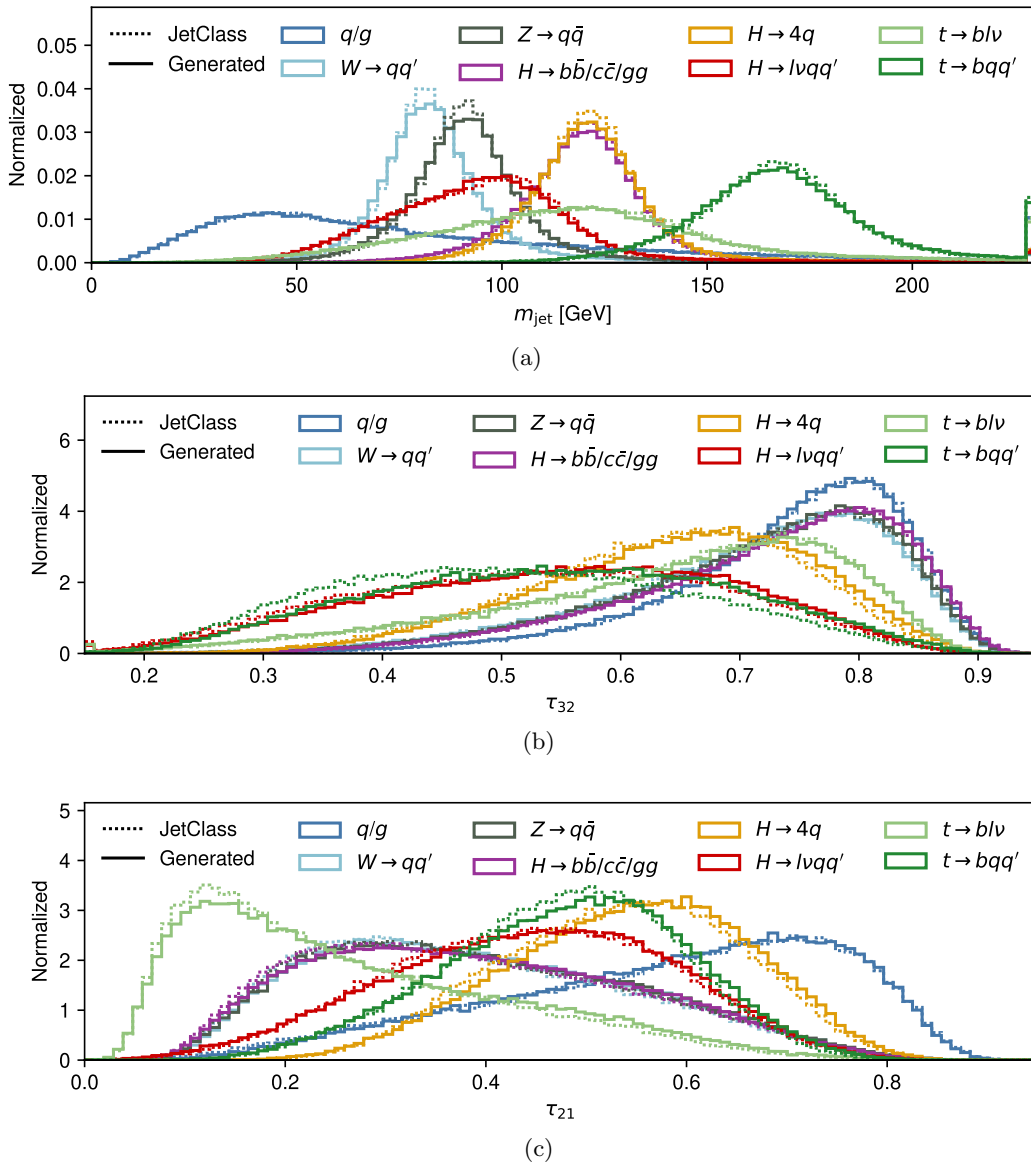


FIG. 5: Jet mass (a) and subjeettiness ratios τ_{32} (b) and τ_{21} (c) for all ten jet types. The histograms in dotted lines show the distributions obtained from the JETCLASS dataset (i.e. real jets) and the solid lines show the histograms obtained from the generated jets. Jets from the categories $H \rightarrow b\bar{b}$, $H \rightarrow c\bar{c}$ and $H \rightarrow gg$ are grouped into one joint histogram for better readability, since the individual histograms show very similar shapes.

B. Jet substructure modeling

The jet mass m_{jet} and the two subjeettiness ratios τ_{32} and τ_{21} are shown in Figure 5 for the different jet types. The real jets are shown in dotted lines while the generated jets are shown in solid lines. Both the jet mass and the subjeettiness ratio distributions show very good agreement for all jet types. The largest deviations between the target distribution and the distribution of the generated jets are seen for $t \rightarrow bqq'$ and $H \rightarrow \ell\nu qq'$, where the distribution of the generated jets peaks at a larger value of τ_{32} . This mismodeling also shows in the values of the KL divergence which are listed in Table III for some of the jet-level observables. Further stud-

ies were done to determine whether narrowing down our model's features to just kinematics and whether training solely on $t \rightarrow bqq'$ jets enhances the modeling of the $t \rightarrow bqq'$ substructure, which can be found in the Appendix in Section C.

C. Classifier test

In addition to the evaluation presented in the previous subsections, we also investigate the performance of our model with the classifier test proposed in Ref. [41]. Thus, a binary classifier is trained to distinguish between real jets from the JETCLASS dataset and fake jets that were generated with our

TABLE III: Kullback-Leibler divergence of jet-level observables with respect to the JETCLASS dataset.

	$ \text{KL}^{m_{\text{jet}}} (\times 10^{-3}) $	$ \text{KL}^{\tau_{21}} (\times 10^{-3}) $	$ \text{KL}^{\tau_{32}} (\times 10^{-3}) $	$ \text{KL}^{D_2} (\times 10^{-3}) $
Truth (q/g)	2.0 ± 0.2	1.9 ± 0.3	2.0 ± 0.3	1.9 ± 0.4
EPiC-FM (q/g)	2.0 ± 0.3	4.3 ± 0.5	2.3 ± 0.2	4.7 ± 0.4
Truth ($H \rightarrow b\bar{b}$)	1.9 ± 0.2	2.0 ± 0.2	2.1 ± 0.2	2.0 ± 0.2
EPiC-FM ($H \rightarrow b\bar{b}$)	3.3 ± 0.5	3.6 ± 0.6	2.7 ± 0.4	3.3 ± 0.5
Truth ($H \rightarrow c\bar{c}$)	2.0 ± 0.3	2.0 ± 0.2	2.2 ± 0.3	1.9 ± 0.2
EPiC-FM ($H \rightarrow c\bar{c}$)	4.8 ± 0.5	6.4 ± 0.6	3.1 ± 0.5	3.7 ± 0.5
Truth ($H \rightarrow gg$)	2.0 ± 0.2	1.8 ± 0.3	1.9 ± 0.2	2.0 ± 0.2
EPiC-FM ($H \rightarrow gg$)	3.8 ± 0.4	3.8 ± 0.6	2.7 ± 0.4	3.2 ± 0.5
Truth ($H \rightarrow 4q$)	2.2 ± 0.4	2.1 ± 0.3	2.0 ± 0.3	1.9 ± 0.3
EPiC-FM ($H \rightarrow 4q$)	5.2 ± 0.5	5.1 ± 0.5	7.8 ± 0.7	3.2 ± 0.5
Truth ($H \rightarrow \ell\nu qq'$)	1.9 ± 0.3	1.9 ± 0.3	2.0 ± 0.2	2.0 ± 0.2
EPiC-FM ($H \rightarrow \ell\nu qq'$)	3.5 ± 0.5	3.5 ± 0.5	9.1 ± 0.9	2.3 ± 0.3
Truth ($Z \rightarrow q\bar{q}$)	2.1 ± 0.2	2.0 ± 0.3	1.9 ± 0.2	2.0 ± 0.2
EPiC-FM ($Z \rightarrow q\bar{q}$)	4.8 ± 0.5	3.5 ± 0.5	2.0 ± 0.2	2.4 ± 0.2
Truth ($W \rightarrow qq'$)	2.1 ± 0.4	2.0 ± 0.2	2.0 ± 0.2	2.0 ± 0.2
EPiC-FM ($W \rightarrow qq'$)	5.8 ± 0.5	4.2 ± 0.6	2.6 ± 0.4	3.1 ± 0.5
Truth ($t \rightarrow bqq'$)	1.9 ± 0.2	2.0 ± 0.3	2.1 ± 0.2	1.9 ± 0.3
EPiC-FM ($t \rightarrow bqq'$)	4.7 ± 0.6	7.9 ± 0.9	30 ± 1	3.0 ± 0.4
Truth ($t \rightarrow b\ell\nu$)	2.0 ± 0.1	1.9 ± 0.2	2.0 ± 0.2	2.0 ± 0.3
EPiC-FM ($t \rightarrow b\ell\nu$)	3.4 ± 0.2	5.8 ± 0.5	2.6 ± 0.4	3.8 ± 0.5

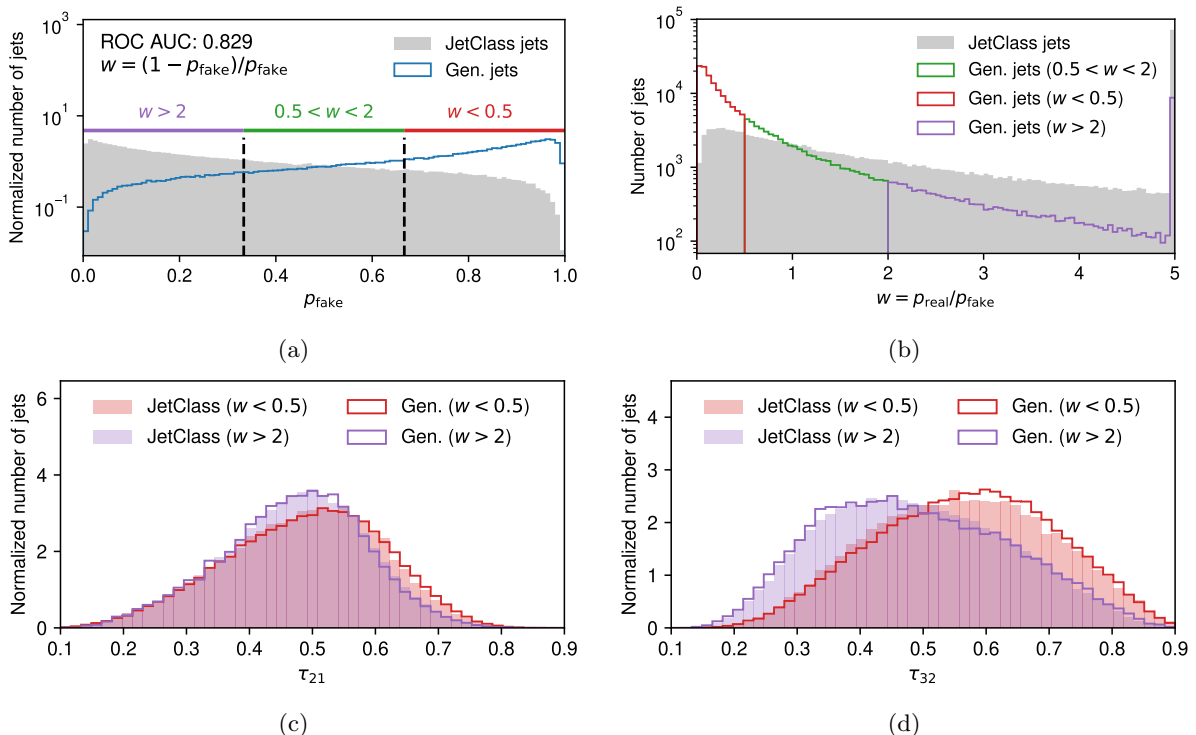


FIG. 6: Results of the classifier test for $t \rightarrow bqq'$ jets. Figure (a) shows the classifier output for real and fake jets, as well as the cut values for the three regions. Figure (b) shows the weight distribution of the fake jets with differently colored histograms for the fake jets from the different regions. Figures (c) and (d) show the τ_{21} and τ_{32} distributions for the real jets and the fake jets from the regions where the classifier output distribution is dominated by real jets or fake jets.

TABLE IV: AUC scores of the classifier test for the ten different jet types.

Jet type	AUC score
q/g	0.681
$W \rightarrow qq'$	0.683
$Z \rightarrow q\bar{q}$	0.689
$H \rightarrow \ell\nu qq'$	0.706
$t \rightarrow b\ell\nu$	0.706
$H \rightarrow b\bar{b}$	0.712
$H \rightarrow gg$	0.716
$H \rightarrow c\bar{c}$	0.728
$H \rightarrow 4q$	0.809
$t \rightarrow bqq'$	0.829

model. This classifier test is performed for each jet type separately.

To train the classifier, we use the 500k fake jets and 500k real jets from the previous evaluation, and split them into 250k, 50k and 200k jets for training, validation and testing of the classifier, respectively. The classifier is trained by fine-tuning the ParT-kin version from Ref. [45], which means that the last MLP of the ParT architecture is re-initialized and changed to two output nodes. The classifier is then trained with real vs fake jets using the AdamW optimizer [50] with a learning rate of 0.001 for a few epochs. However, it should be noted that the classifier training was not extensively optimized. We noticed that the validation loss converges after just a few epochs after which the classifier starts to overfit. We therefore chose to use the model with the highest validation accuracy before clear signs of overfitting are visible.

The AUC values of the corresponding ROC curves are shown in Table IV. To estimate the uncertainty of the classifier scores, five classifiers are trained for $H \rightarrow b\bar{b}$ jets with different random seeds. All classifiers converge at similar performance, with the standard deviation of the AUC scores being $\sigma_{\text{AUC}}(H \rightarrow b\bar{b}) = 0.003$.

The largest AUC value is obtained for $t \rightarrow bqq'$ jets with an AUC of 0.829, confirming again that this is the most challenging jet type for our model. The results of the corresponding classifier test are shown in Figure 6 in more detail. However, the AUC value for $t \rightarrow bqq'$ jets is still well below 1, allowing us to investigate the $t \rightarrow bqq'$ jets corresponding to different regions of the classifier output. Therefore, following Ref. [42], we split the $t \rightarrow bqq'$ jets into three regions, based on their weight $w = p_{\text{real}}/p_{\text{fake}}$ as illustrated in Figure 6a and Figure 6b. The first region contains jets with $w > 2$, the second region contains jets with $0.5 < w < 2$, and the third region contains jets with $w < 0.5$. Thus, the outer regions correspond to jets that are clearly identified as either real or fake jets, while the center region contains jets where the classifier is not able to clearly distinguish them.

The corresponding subjettness ratios τ_{21} and τ_{32} are shown in Figure 6c and Figure 6d for $t \rightarrow bqq'$

jets from the outer regions. This shows the jet substructure differences between the $t \rightarrow bqq'$ jets that are clearly classified as either real or fake. $t \rightarrow bqq'$ jets that correspond to $w > 2$, i.e. jets of which the classifier is rather certain that they are real jets, have on average a smaller τ_{32} value than $t \rightarrow bqq'$ jets that are clearly identified as fake jets ($w < 0.5$). Therefore, the classifier classifies $t \rightarrow bqq'$ jets that are more 3-prong-like (i.e. with a smaller τ_{32} value) as real $t \rightarrow bqq'$ jets, while $t \rightarrow bqq'$ jets that are less 3-prong-like (i.e. with a larger τ_{32} value) tend to be classified as fake $t \rightarrow bqq'$ jets. Thus, our model seems to struggle with the modeling of the 3-prong structure of $t \rightarrow bqq'$ jets, which is also consistent with the results from the previous sections, where we saw that the τ_{32} distribution of the generated $t \rightarrow bqq'$ jets peaks at a slightly larger value than the τ_{32} distribution of the real $t \rightarrow bqq'$ jets. The peak at the larger τ_{32} value and thus the overall shift of the distribution is caused by the poorly modeled jets: given that 61% of the fake $t \rightarrow bqq'$ jets have $w < 0.5$, the overall τ_{32} distribution of the fake jets is dominated by jets with larger τ_{32} . On the other hand, only 15% of the real $t \rightarrow bqq'$ jets have $w < 0.5$, and 58% of the real $t \rightarrow bqq'$ jets have $w > 2$, which correspond to the purple distribution in Figure 6d.

V. CONCLUSION

Generative surrogate models of different physical processes are a powerful new tool with multiple potential applications. So far, speeding up classical simulations, either of particle interactions in calorimeters or of the calculation of matrix elements, has been the primary focus of research. However, learning surrogate models of jets has its own interesting aspects: i) such models can, in principle, be trained on collider data, allowing the interpolation of distributions to estimate backgrounds; ii) they can form parts of a fully differentiable analysis and interpretation chain; iii) an interpretable version trained directly on collider data may provide an additional way of gaining insight into showering and hadronization processes; iv) learning jets at the constituent level is a crucial stepping stone to simulating full events at the finest granularity; and v) they provide a meaningful testbed to benchmark progress in generative models for point clouds.

The main result of this work is that the EPiC-FM [14] framework can be easily scaled up to more complex datasets. The move from the JETNET to the JETCLASS dataset results in more classes (10 instead of 5), more features per jet (13 instead of 3), geometrically larger jets ($R = 0.8$ instead of $R = 0.4$), and finally more jets available for training with JETCLASS containing a factor of 70 more jets per jet type than JETNET.

Overall we observe an accurate description of physical quantities. For some individual features and classes, the agreement between generated data and

ground truth is on the same level as the statistical fluctuations between different samples drawn from the ground truth distribution. In general, more complex final states (i.e. multi-pronged signals with intermediate resonances) are more difficult to describe than relatively simple light quark or gluon-induced jets.

The capability to model quantities beyond jet kinematics demonstrated here will serve as an important factor in further increasing the performance of anomaly detection algorithms. Previous results already showed that going from a few high-level to many low-level features increases the maximum achievable significance improvement by more than a factor of three [4]. Access to trajectory displacement and particle identification quantities now enable these models to be sensitive to final states including b -flavor and for example allow automatically covering long-lived [56] final states with anomaly detection as well, greatly increasing their accessible theory phase space.

Finally, the JETCLASS dataset has sufficient complexity to serve as a useful next benchmark for generative models applied to point-cloud-like data. Accordingly, we provide an extensive set of one-dimensional (KL-divergences) and multi-dimensional (classifier scores) evaluation methods for future reference and comparison.

CODE AVAILABILITY

The code used to produce the results presented in this paper is available at https://github.com/uhh-pd-ml/beyond_kinematics.

ACKNOWLEDGEMENTS

The authors thank Huilin Qu for his support with the JETCLASS dataset and helping with any questions. EB is funded by a scholarship of the Friedrich Naumann Foundation for Freedom and by the German Federal Ministry of Science and Research (BMBF) via Verbundprojekts 05H2018 - R&D COMPUTING (Pilotmaßnahme ErUM-Data) Innovative Digitale Technologien für die Erforschung von Universum und Materie. JB, EB, CE, and GK acknowledge support by the Deutsche Forschungsgemeinschaft under Germany's Excellence Strategy – EXC 2121 Quantum Universe – 390833306 and via the KISS consortium (05D23GU4) funded by the German Federal Ministry of Education and Research BMBF in the ErUM-Data action plan. DS is supported by DOE grant DOE-SC0010008. This research was supported in part through the Maxwell computational resources operated at Deutsches Elektronen-Synchrotron DESY, Hamburg, Germany.

-
- [1] T. Sjöstrand, S. Ask, J. R. Christiansen, R. Corke, N. Desai, P. Ilten, S. Mrenna, S. Prestel, C. O. Rasmussen, and P. Z. Skands, *Computer Physics Communications* **191**, 159–177 (2015).
 - [2] M. Bähr, S. Gieseke, M. A. Gigg, D. Grellscheid, K. Hamilton, O. Latunde-Dada, S. Plätzer, P. Richardson, M. H. Seymour, A. Sherstnev, and B. R. Webber, *The European Physical Journal C* **58**, 639–707 (2008).
 - [3] L. Evans and P. Bryant, *JINST* **3**, S08001 (2008).
 - [4] E. Buhmann, C. Ewen, G. Kasieczka, V. Mikuni, B. Nachman, and D. Shih, “Full Phase Space Resonant Anomaly Detection,” (2023), [arXiv:2310.06897 \[hep-ph\]](https://arxiv.org/abs/2310.06897).
 - [5] R. Kansal, J. Duarte, H. Su, B. Orzari, T. Tomei, M. Pierini, M. Touranakou, J.-R. Vlimant, and D. Gunopulos, “Particle Cloud Generation with Message Passing Generative Adversarial Networks,” (2022), [arXiv:2106.11535 \[cs.LG\]](https://arxiv.org/abs/2106.11535).
 - [6] B. Käch, D. Krücker, I. Melzer-Pellmann, M. Scham, S. Schnake, and A. Verney-Provatas, “Jet-Flow: Generating Jets with Conditioned and Mass Constrained Normalising Flows,” (2022), [arXiv:2211.13630 \[hep-ex\]](https://arxiv.org/abs/2211.13630).
 - [7] E. Buhmann, G. Kasieczka, and J. Thaler, “EPiC-GAN: Equivariant Point Cloud Generation for Particle Jets,” (2023), [arXiv:2301.08128 \[hep-ph\]](https://arxiv.org/abs/2301.08128).
 - [8] M. Leigh, D. Sengupta, G. Quétant, J. A. Raine, K. Zoch, and T. Golling, “PC-JeDi: Diffusion for Particle Cloud Generation in High Energy Physics,” (2023), [arXiv:2303.05376 \[hep-ph\]](https://arxiv.org/abs/2303.05376).
 - [9] V. Mikuni, B. Nachman, and M. Pettee, “Fast Point Cloud Generation with Diffusion Models in High Energy Physics,” (2023), [arXiv:2304.01266 \[hep-ph\]](https://arxiv.org/abs/2304.01266).
 - [10] B. Käch and I. Melzer-Pellmann, “Attention to Mean-Fields for Particle Cloud Generation,” (2023), [arXiv:2305.15254 \[hep-ex\]](https://arxiv.org/abs/2305.15254).
 - [11] E. Buhmann, S. Diefenbacher, E. Eren, F. Gaede, G. Kasieczka, A. Korol, W. Korcari, K. Krüger, and P. McKeown, “CaloClouds: Fast Geometry-Independent Highly-Granular Calorimeter Simulation,” (2023), [arXiv:2305.04847 \[physics.ins-det\]](https://arxiv.org/abs/2305.04847).
 - [12] M. Leigh, D. Sengupta, J. A. Raine, G. Quétant, and T. Golling, “PC-Droid: Faster diffusion and improved quality for particle cloud generation,” (2023), [arXiv:2307.06836 \[hep-ex\]](https://arxiv.org/abs/2307.06836).
 - [13] E. Buhmann, F. Gaede, G. Kasieczka, A. Korol, W. Korcari, K. Krüger, and P. McKeown, “CaloClouds II: Ultra-Fast Geometry-Independent Highly-Granular Calorimeter Simulation,” (2023), [arXiv:2309.05704 \[physics.ins-det\]](https://arxiv.org/abs/2309.05704).
 - [14] E. Buhmann, C. Ewen, D. A. Faroughy, T. Golling, G. Kasieczka, M. Leigh, G. Quétant, J. A. Raine, D. Sengupta, and D. Shih, “EPiC-ly Fast Particle Cloud Generation with Flow-Matching and Diffusion,” (2023), [arXiv:2310.00049 \[hep-ph\]](https://arxiv.org/abs/2310.00049).
 - [15] A. Vaswani *et al.*, in *Proceedings of Advances in Neural Information Processing Systems*, Vol. 30 (2017) pp. 5999–6009, 1706.03762.
 - [16] J. Sohl-Dickstein, E. A. Weiss, N. Maheswaranathan, and S. Ganguli, “Deep Unsupervised Learning using Nonequilibrium Thermodynamics,” (2015), [arXiv:1503.03585 \[cs.LG\]](https://arxiv.org/abs/1503.03585).

- [17] Y. Song and S. Ermon, “Generative Modeling by Estimating Gradients of the Data Distribution,” (2020), [arXiv:1907.05600 \[cs.LG\]](#).
- [18] Y. Song and S. Ermon, “Improved Techniques for Training Score-Based Generative Models,” (2020), [arXiv:2006.09011 \[cs.LG\]](#).
- [19] J. Ho, A. Jain, and P. Abbeel, “Denoising Diffusion Probabilistic Models,” (2020), [arXiv:2006.11239 \[cs.LG\]](#).
- [20] Y. Song, J. Sohl-Dickstein, D. P. Kingma, A. Kumar, S. Ermon, and B. Poole, “Score-Based Generative Modeling through Stochastic Differential Equations,” (2021), [arXiv:2011.13456 \[cs.LG\]](#).
- [21] X. Liu, C. Gong, and Q. Liu, “Flow Straight and Fast: Learning to Generate and Transfer Data with Rectified Flow,” (2022), [arXiv:2209.03003 \[cs.LG\]](#).
- [22] M. S. Albergo and E. Vanden-Eijnden, “Building Normalizing Flows with Stochastic Interpolants,” (2023), [arXiv:2209.15571 \[cs.LG\]](#).
- [23] Y. Lipman, R. T. Q. Chen, H. Ben-Hamu, M. Nickel, and M. Le, “Flow Matching for Generative Modeling,” (2023), [arXiv:2210.02747 \[cs.LG\]](#).
- [24] A. Tong, N. Malkin, G. Huguët, Y. Zhang, J. Rector-Brooks, K. Fatras, G. Wolf, and Y. Bengio, “Improving and generalizing flow-based generative models with minibatch optimal transport,” (2023), [arXiv:2302.00482 \[cs.LG\]](#).
- [25] S. Agostinelli *et al.*, Nuclear Instruments and Methods in Physics Research Section A: Accelerators, Spectrometers, Detectors and Associated Equipment **506**, 250 (2003).
- [26] J. Allison *et al.*, IEEE Trans. Nucl. Sci. **53**, 270 (2006).
- [27] J. Allison *et al.*, Nuclear Instruments and Methods in Physics Research Section A: Accelerators, Spectrometers, Detectors and Associated Equipment **835**, 186 (2016).
- [28] F. T. Acosta, V. Mikuni, B. Nachman, M. Aratia, B. Karki, R. Milton, P. Karande, and A. Angerami, “Comparison of point cloud and image-based models for calorimeter fast simulation,” (2023), [arXiv:2307.04780 \[cs.LG\]](#).
- [29] M. A. W. Scham, D. Krücker, B. Käch, and K. Borrás, “DeepTreeGAN: Fast Generation of High Dimensional Point Clouds,” (2023), [arXiv:2311.12616 \[hep-ex\]](#).
- [30] S. Otten, S. Caron, W. de Swart, M. van Beekveld, L. Hendriks, C. van Leeuwen, D. Podareanu, R. Ruiz de Austri, and R. Verheyen, Nature Commun. **12**, 2985 (2021), [arXiv:1901.00875 \[hep-ph\]](#).
- [31] B. Hashemi, N. Amin, K. Datta, D. Olivito, and M. Pierini, “LHC analysis-specific datasets with Generative Adversarial Networks,” (2019), [arXiv:1901.05282 \[hep-ex\]](#).
- [32] R. Di Sipio, M. Fauci Giannelli, S. Ketabchi Haghighat, and S. Palazzo, JHEP **08**, 110 (2019), [arXiv:1903.02433 \[hep-ex\]](#).
- [33] A. Butter, T. Plehn, and R. Winterhalder, SciPost Phys. **7**, 075 (2019), [arXiv:1907.03764 \[hep-ph\]](#).
- [34] Y. Alanazi, N. Sato, T. Liu, W. Melnitchouk, P. Ambrozewicz, F. Hauenstein, M. P. Kuchera, E. Pritchard, M. Robertson, R. Strauss, L. Velasco, and Y. Li, in *Proceedings of the Thirtieth International Joint Conference on Artificial Intelligence, IJCAI-21*, edited by Z.-H. Zhou (IJCAI, 2021) p. 2126, [2001.11103](#).
- [35] A. Butter, T. Heimel, S. Hummerich, T. Krebs, T. Plehn, A. Rousselot, and S. Vent, “Generative Networks for Precision Enthusiasts,” (2021), [arXiv:2110.13632 \[hep-ph\]](#).
- [36] A. Butter, N. Huetsch, S. P. Schweitzer, T. Plehn, P. Sorrenson, and J. Spinner, “Jet Diffusion versus JetGPT – Modern Networks for the LHC,” (2023), [arXiv:2305.10475 \[hep-ph\]](#).
- [37] A. Butter, T. Jezo, M. Klasen, M. Kuschick, S. P. Schweitzer, and T. Plehn, “Kicking it Off(-shell) with Direct Diffusion,” (2023), [arXiv:2311.17175 \[hep-ph\]](#).
- [38] R. Kansal, J. Duarte, H. Su, B. Orzari, T. Tomei, M. Pierini, M. Touranakou, J.-R. Vlimant, and D. Gunopulos, “JetNet,” (2022).
- [39] R. Kansal, J. Duarte, H. Su, B. Orzari, T. Tomei, M. Pierini, M. Touranakou, J.-R. Vlimant, and D. Gunopulos, “JetNet150,” (2022).
- [40] E. Coleman, M. Freytsis, A. Hinzmann, M. Narain, J. Thaler, N. Tran, and C. Vernieri, JINST **13**, T01003 (2018).
- [41] C. Krause and D. Shih, Physical Review D **107** (2023), [10.1103/physrevd.107.113003](#).
- [42] R. Das, L. Favaro, T. Heimel, C. Krause, T. Plehn, and D. Shih, “How to Understand Limitations of Generative Networks,” (2023), [arXiv:2305.16774 \[hep-ph\]](#).
- [43] H. Qu, C. Li, and S. Qian, “JetClass: A Large-Scale Dataset for Deep Learning in Jet Physics,” (2022).
- [44] R. T. Q. Chen, Y. Rubanova, J. Bettencourt, and D. Duvenaud, “Neural Ordinary Differential Equations,” (2019), [arXiv:1806.07366 \[cs.LG\]](#).
- [45] H. Qu, C. Li, and S. Qian, in *Proceedings of the 39th International Conference on Machine Learning* (2022) pp. 18281–18292, [arXiv:2202.03772 \[hep-ph\]](#).
- [46] J. Alwall, R. Frederix, S. Frixione, V. Hirschi, F. Maltoni, O. Mattelaer, H.-S. Shao, T. Stelzer, P. Torrielli, and M. Zaro, Journal of High Energy Physics **2014** (2014), [10.1007/jhep07\(2014\)079](#).
- [47] J. de Favereau, C. Delaere, P. Demin, A. Giamanco, V. Lemaitre, A. Mertens, and M. Selvaggi, Journal of High Energy Physics **2014** (2014), [10.1007/jhep02\(2014\)057](#).
- [48] The CMS Collaboration, JINST **3**, S08004 (2008).
- [49] M. Cacciari, G. P. Salam, and G. Soyez, Journal of High Energy Physics **2008**, 063–063 (2008).
- [50] I. Loshchilov and F. Hutter, “Decoupled Weight Decay Regularization,” (2019), [arXiv:1711.05101 \[cs.LG\]](#).
- [51] A. Paszke *et al.*, in *Advances in Neural Information Processing Systems 32*, edited by H. Wallach, H. Larochelle, A. Beygelzimer, F. d’Alché-Buc, E. Fox, and R. Garnett (Curran Associates, Inc., 2019) pp. 8024–8035.
- [52] W. Falcon and The PyTorch Lightning team, “PyTorch Lightning,” (2019).
- [53] J. Thaler and K. V. Tilburg, JHEP **03**, 015 (2011).
- [54] A. J. Larkoski, I. Moulton, and D. Neill, “Analytic Boosted Boson Discrimination,” (2016), [arXiv:1507.03018 \[hep-ph\]](#).
- [55] A. J. Larkoski, G. P. Salam, and J. Thaler, JHEP **06**, 108 (2013).
- [56] J. Alimena *et al.*, Journal of Physics G: Nuclear and Particle Physics **47**, 090501 (2020).

Appendix A: Modeling of the electric charge

Similar to the evaluation of the particle-ID features, we show the average number of jet constituents corresponding to different electric charge values in Figure 7.

While the spread is quite large as indicated by the intervals in Figure 7, around half of the jet constituents are electrically neutral and correspondingly around a quarter of the constituents carries charge -1 and 1 , respectively.

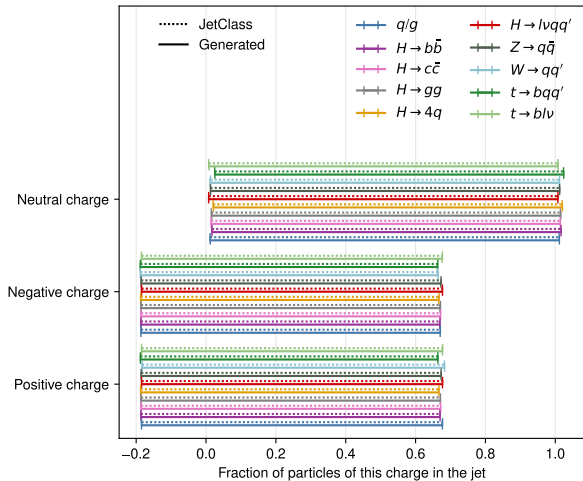


FIG. 7: Average fraction of jet constituents of different electric charge. For each jet type, the intervals show the mean value over all evaluated jets with up and down variations of one standard deviation. The dotted lines show the values obtained for real jets from the JETCLASS dataset and the solid lines show the values obtained for the generated jets.

Appendix B: Hyperparameters

The hyperparameters used for our generative model are listed in Table V. This choice of hyperparameters was found to lead to the best performance among several different configurations, though they were not extensively optimized.

The hyperparameters used for the classifier test are shown in Table VI. The model weights are initialized using the pre-trained ParT-kin model from https://github.com/jet-universe/particle_transformer.

Appendix C: Further studies for hadronic top jet modeling

Since $t \rightarrow bqq'$ jets were found to be the most challenging jet type to model, further studies are performed to improve and investigate the modeling of those jets. To this end, we compare our baseline model, which we refer to in the following as EPiC-FM, to three additional models:

TABLE V: Hyperparameters used for the baseline EPiC-FM model.

Hyperparameter	Value
Number of EPiC layers	20
Global dim. in EPiC layers	16
Hidden dim. in EPiC layers	300
ODE solver	midpoint
Number of function evaluations	200
Activation function	LeakyReLU(0.01)
AdamW [50] learning rate	0.001
Weight decay	0.00005
Learning rate scheduler	CosineAnnealing
Linear warm-up	20 epochs
Total number of epochs	EPiC-FM: 500
	EPiC-FM-kin: 500
	EPiC-FM-top: 1000
	EPiC-FM-kintop: 1000
Batch size	1024
Trainable parameters	8,504,698
Training jets	3M (300k per jet type)

TABLE VI: Hyperparameters used for the classifier test with the ParT-kin [45] model.

Hyperparameter	Value
AdamW [50] learning rate	0.001
Weight decay	0.00005
Learning rate scheduler	Constant
Total number of epochs	100
Batch size	256
Trainable parameters	2 141 134
Training jets	500 000
Validation jets	100 000
Testing jets	400 000

- **EPiC-FM-top** is trained on the same features as the baseline model, but only the $t \rightarrow bqq'$ jets from the training dataset are used for training;
- **EPiC-FM-kin** is trained on kinematic features only (i.e. p_T^{rel} , η^{rel} and ϕ^{rel}) but uses the full training dataset and
- **EPiC-FM-kintop** is trained on kinematic features only (i.e. p_T^{rel} , η^{rel} and ϕ^{rel}) and only uses the $t \rightarrow bqq'$ jets from the training dataset.

The KL divergence values for the jet-level observables are listed for all models in Table VII and the substructure of the generated $t \rightarrow bqq'$ jets for the three different models is shown in Figure 8. It can be seen that the models that are restricted to kinematic features show better agreement with the real jets than the two models that are trained on all features. This is also confirmed by the KL divergence, which show that the EPiC-FM-kin model has a significantly smaller KL divergence than the EPiC-FM model for all substructure observables. These observations lead to the conclusion that the additional features slightly confuse the modeling of the kinematic features which results in a worse representation of

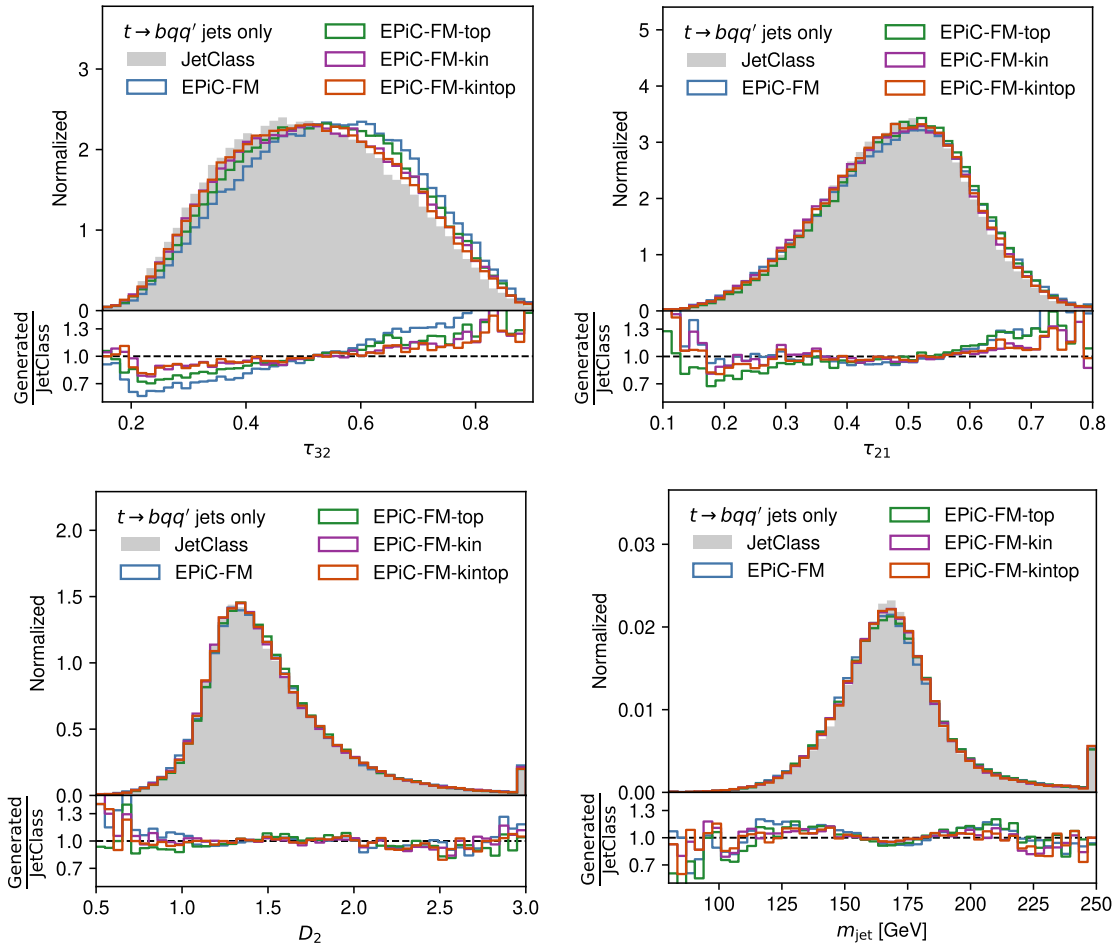


FIG. 8: Comparison of the jet substructure of $t \rightarrow bqq'$ jets for the four different models. The models EPiC-FM-top and EPiC-FM-kintop were trained on $t \rightarrow bqq'$ jets only.

TABLE VII: KL divergence metrics for the four different models used for improving the modeling of $t \rightarrow bqq'$ jets. The models EPiC-FM-top and EPiC-FM-kintop were trained on $t \rightarrow bqq'$ jets only.

	$ \text{KL}^{m_{\text{jet}}} (\times 10^{-3}) $	$ \text{KL}^{\tau_{21}} (\times 10^{-3}) $	$ \text{KL}^{\tau_{32}} (\times 10^{-3}) $	$ \text{KL}^{D_2} (\times 10^{-3}) $
Truth ($t \rightarrow bqq'$)	1.9 ± 0.2	2.0 ± 0.3	2.1 ± 0.2	1.9 ± 0.3
EPiC-FM ($t \rightarrow bqq'$)	4.7 ± 0.6	7.9 ± 0.9	30 ± 1	3.0 ± 0.4
EPiC-FM-kin ($t \rightarrow bqq'$)	2.7 ± 0.3	3.2 ± 0.4	6.2 ± 0.8	2.1 ± 0.3
EPiC-FM-top ($t \rightarrow bqq'$)	4.3 ± 0.4	7.8 ± 0.6	13.3 ± 0.9	3.1 ± 0.3
EPiC-FM-kintop ($t \rightarrow bqq'$)	2.6 ± 0.4	3.5 ± 0.3	4.8 ± 0.6	2.3 ± 0.3

the substructure. However, the jets are still modeled well in the case of all features, and the ability to model the discrete features extends the usability of such generative models.

The model that is restricted to $t \rightarrow bqq'$ jets and kinematic features, EPiC-FM-kintop, shows similar improvements as the EPiC-FM-kin model. However, while there is a slight improvement over the EPiC-FM-kin model in the KL divergence for τ_{32} , the KL divergence for τ_{21} and D_2 is slightly larger than for

the kin-only model. In the case where all features are used, i.e. when comparing the EPiC-FM-top model to the baseline model EPiC-FM, we see an improvement in τ_{32} , while not seeing an improvement in the KL divergence of τ_{21} and D_2 . Thus, the single jet-type model performs better than the model that is trained on all jet types if all features are used, while there is no clear improvement by training solely on $t \rightarrow bqq'$ jets if only kinematic features are used.